
Numerical Modeling and Control of Multifrequency Atomic Force Microscopy

By

D. JOHANN DJANAL-MANN



Department of Engineering Mathematics
UNIVERSITY OF BRISTOL

A dissertation submitted to the University of Bristol in accordance with the requirements of the degree of MASTER OF SCIENCE in the Faculty of Engineering.

SEPTEMBER 2020

ABSTRACT

The atomic Force Microscope (AFM) is a microelectromechanical device capable of characterizing a specimen with a nanoscale physical probe, made up of a cantilever with a sharp tip at one end. When the tip is close to the surface (on the order of nanometers), it moves in response to atomic forces, resulting in a deflection of the cantilever that can be detected via, e.g., a laser and photodiode. This allows the AFM to provide a 3D surface profile at the atomic scale, measure a range of material properties in addition to topography, while eliminating the requirement for samples to undergo special treatment or be placed in a vacuum environment. It is hence ideal for imaging biological and other delicate specimen.

Due to the nonlinear motion of the cantilever, information about the atomic processes that is encoded in the deflection at frequencies other than the excitation frequency is irreversibly lost [3]. Neglecting these frequencies also restricts the number of visualization channels [3]. This led to the development of multifrequency atomic force microscopy (MF-AFM), which involves the excitation and/or detection of the deflection at two or more frequencies. The advancement of the instrument in general, will depend on improved and detailed knowledge of the cantilever's vibrational properties in these extended modes.

This project aims to study the AFM's response to current standard control techniques under multifrequency operation, as well as categorize its nonlinear dynamics. It includes a description of potential applications and an overview of the latest developments in the field.

DEDICATION AND ACKNOWLEDGEMENTS

The dedication of this report is split 4 ways:

T

To my supervisor, Dr. Martin Homer, whose feedback and resourcefulness was a great source of encouragement and motivation.

To Dr. Marco Corragio, whose patience and enlightenment contributed greatly towards my comprehension.

To the technical support staff at MathWorks, Inc., whose assistance with debugging code is immeasurably appreciated.

And to my family, whose support and love made this possible to begin with.

AUTHOR'S DECLARATION

I declare that the work in this dissertation was carried out in accordance with the requirements of the University's Regulations and Code of Practice for Research Degree Programmes and that it has not been submitted for any other academic award. Except where indicated by specific reference in the text, the work is the candidate's own work. Work done in collaboration with, or with the assistance of, others, is indicated as such. Any views expressed in the dissertation are those of the author.

SIGNED: ..DOMINIQUE JOHANN DJANAL-MANN.....

DATE:18 SEPTEMBER 2020.....

TABLE OF CONTENTS

	Page
List of Figures	v
List of Tables	vii
1 Introduction	1
1.1 Operation	2
1.2 Multifrequency AFM	3
1.2.1 Applications	4
1.3 Objectives	5
2 Literature Review	6
2.1 Mathematical Models	6
2.1.1 Cantilever	6
2.1.2 Tip-Sample Forces	7
2.2 Nonlinear Dynamics	9
2.3 Control Techniques	10
2.4 Bimodal AFM	11
3 Project Model	13
3.1 Single Mode	13
3.2 Multifrequency	15
3.3 Control Strategy	15
4 Results	17
4.1 Calculations	17
4.2 Analysis	20
5 Conclusion	31

LIST OF FIGURES

FIGURE	Page
1.1 AFM configuration. The basic components are the probe, the cantilever, the scanner, the laser, a data processor and a photodetector as shown [2].	2
1.2 Illustration of atomic force microscopy in static (top), dynamic (middle), and multifrequency (bottom) modes [24]	3
2.1 Cantilever modelled as (a) a continuous beam without the tip and (b) a damped harmonic oscillator [13][5]	7
2.2 1st 3 bending modes for rectangular-, picket-, and V-shaped cantilevers and strain energy density contour. Reproduced from [5].	10
3.1 AFM Model: (a) Schematic of the cantilever tip close to the sample surface. (b) Interaction forces according to Derjaguin-Muller-Toporov model (DMT), with coefficient values in Table I. The inset shows the detail of the repulsive forces. Reproduced from [4]	14
4.1 Model Validation (flat surface): (a) 3-D and (b) 2-D topographical plots of the sample. (c) Cantilever trajectory	21
4.2 Model Validation (ramp surface): (a) 3-D and (b) 2-D topographical plots of the sample. (c) Cantilever trajectory	22
4.3 Model Validation (square-wave surface): (a) 3-D and (b) 2-D topographical plots of the sample. (c) Cantilever trajectory	23
4.4 Error response $e_A \approx A_r - A$ with PID gains $K_P = 0.5, K_I = 8.5, K_D = 0$ on the (a) flat surface (4.1b), (b) ramp surface (4.2b), and (c) square-wave surface (4.3b)	24
4.5 Bimodal cantilever solutions of the first flexural mode with stationary base for the (a) flat surface, (b) ramp surface, and (c) square-wave surface.	25
4.6 Bimodal cantilever solutions of the second flexural mode with stationary base for the (a) flat surface, (b) ramp surface, and (c) square-wave surface.	26
4.7 Bimodal response of (a) the first mode and (b) the second mode to PID control with gains $K_P = 0.5, K_I = 8.5$, and $K_D = 0$ on flat sample surface. (c) is error in the amplitude estimation of mode 1.	27

LIST OF FIGURES

4.8 Bimodal response of (a) the first mode and (b) the second mode to PID control with gains $K_P = 0.5$, $K_I = 250$, and $K_D = 0$ on flat sample surface. (c) is error in the amplitude estimation of mode 1.	28
4.9 Cantilever trajectory for monomodal AFM on (a) ramp surface (4.2b), and (b) square-wave surface (4.3b)	29
4.10 (a) Cantilever trajectory and (b) error response, respectively, for monomodal AFM on square-wave surface with $K_P = 0.5, K_I = 3.5, K_D = 0$	30
4.11 (a) Cantilever trajectory and (b) error response, respectively, for monomodal AFM on square-wave surface with $K_P = 0.5, K_I = 0.5, K_D = 0$	30

LIST OF TABLES

TABLE	Page
2.1 van der Waals interaction laws for most common AFM geometry (H is the Hamaker constant, d is the tip-surface distance, R is the radius of the sphere / cylinder, θ is the semi-aperture of the cone, $R_\theta = R(1-\sin\theta)$, and l is the semi-axis of the paraboloid. $H = \pi^2 C \rho_1 \rho_2$, where C is the constant in the atom-atom pair potential and ρ_1 and ρ_2 are the number of atoms per unit volume. The formula for 2 flat surfaces calculates force per unit area [9]).	8
2.2 Equations for contact radius a , sample deformation δ , and adhesion force $F_a d$ for a spherical tip on a flat surface according to Hertz, DMT, and JKR (P is the force exerted by the tip on the surface) [18][5]	9
4.1 Parameters used for the AFM simulations, in accordance with [4]	18
4.2 Parameters for Bimodal Simulations	19

INTRODUCTION

Atomic force microscopy (AFM) is a very-high-resolution type of scanning probe microscopy (SPM), with demonstrated resolution on the order of fractions of a nanometer, more than 1000 times better than the optical diffraction limit [17]. SPM is a branch of microscopy that forms images of surfaces using a physical probe that scans the specimen. Prior to the invention of the SPM, interrogating the structure of material with atomic-scale precision was cumbersome, expensive, and difficult. Since the invention of these instruments, atomic-scale interrogation of matter has become simple and inexpensive. There are several different types of SPM techniques, including scanning tunneling microscopy (STM) and near-field scanning optical microscope (NSOM). What makes AFM unique among competing technologies is its extended capabilities beyond imaging and that it does not require lenses or beam irradiation. Therefore, it does not suffer from a limitation in spatial resolution due to diffraction and aberration, and preparing a space for guiding the beam (by creating a vacuum) and coating the sample are not necessary [22]. AFM can be applied to both conductors and insulators, operated in gas and liquid environments, and achieve improved topographic contrast and surface features.

AFM has three major abilities: force measurement, topographic imaging, and manipulation [29]. In force measurement, AFMs can be used to measure the forces between the probe and the sample as a function of their mutual separation. This can be applied to perform force spectroscopy, to measure the mechanical properties of the sample, such as the sample's Young's modulus, a measure of stiffness. For imaging, the reaction of the probe to the forces that the sample imposes on it can be used to form an image of the three-dimensional shape (topography) of a sample surface at a high resolution [8]. This is achieved by raster scanning the position of the sample with respect to the tip and recording the height of the probe that corresponds to a constant probe-sample interaction. In manipulation, the forces between tip and sample can also be used

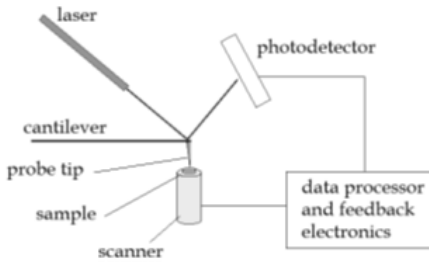


Figure 1.1: AFM configuration. The basic components are the probe, the cantilever, the scanner, the laser, a data processor and a photodetector as shown [2].

to change the properties of the sample in a controlled way. Examples of this include atomic manipulation, scanning probe lithography and local stimulation of cells [20].

1.1 Operation

The general construction of the atomic force microscope is shown in Figure 1.1. Its probe consists of a nanoscale cantilever with a sharp tip protruding at the free end. Optionally, a piezoelectric element, known as the dither piezo, drives the oscillation of the spring-like cantilever. The sample is mounted on a stage. When the tip is within nanometers of the sample surface, it moves in response to atomic interacting forces, resulting in a deflection of the cantilever that can be detected. Various means of detection exists, such as interferometry, optical levers, the piezoresistive method, and the piezoelectric method [29]. The deflection is measured as the displacement with respect to the equilibrium position of the cantilever, which the detector converts into an electrical signal. The intensity of this signal is proportional to the displacement of the cantilever. The movement of the probe assembly or specimen in the x -, y -, and z -directions is controlled by a piezoelectric tube scanner [12].

The AFM can be operated in a number of modes, according to the nature of the tip motion and depending on the application. In general, imaging may be operated in contact or non-contact mode, depending on whether the tip apex is penetrating the repulsive part of the interaction potential of the tip/sample system. Static and dynamic modes of operation are distinguished depending on whether the cantilever is oscillating or not [2].

Static mode (or contact mode) is the original and simplest mode to operate an AFM. In this mode, the probe is in continuous contact with the sample while the probe raster scans the surface. The force F_{ts} which acts between the tip and sample is used as the imaging signal. In the static mode, the force translates into a deflection $\delta x = F_{ts}/k$ of the cantilever, where k is its force constant [6]. In the dynamic operation modes, the cantilever is deliberately vibrated. The cantilever is mounted on an actuator, the dither piezo, to allow the external excitation of an oscillation. When the tip approaches the sample, elastic and inelastic interactions cause a change in both the amplitude and the phase (relative to the driving signal) of the cantilever.

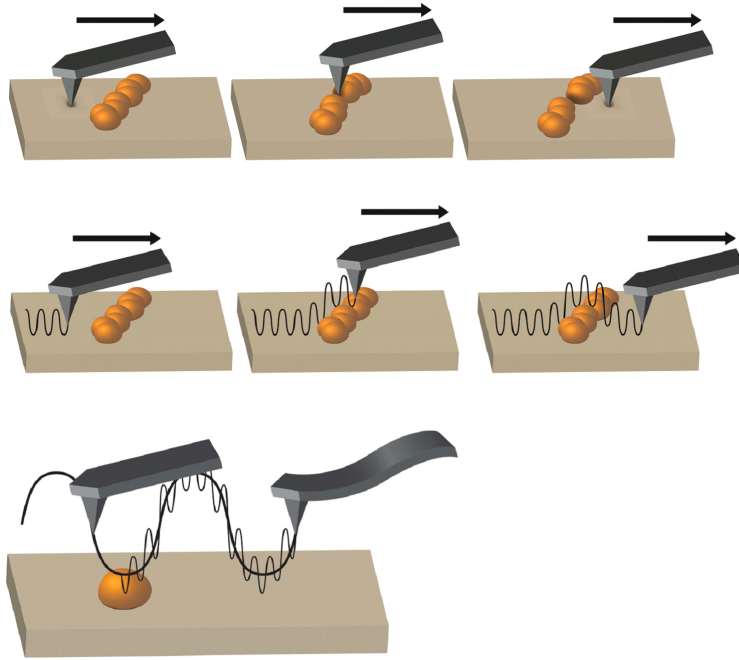


Figure 1.2: Illustration of atomic force microscopy in static (top), dynamic (middle), and multifrequency (bottom) modes [24]

These changes are used as the feedback signal. The purpose of any dynamic AFM experiment is to recover the information about the sample's properties encoded in the cantilever dynamics. The cantilever dynamics are inherently nonlinear because the amplitude of the oscillation is higher than the decay lengths of the interaction forces, putting the tip under the influence of the surface only during a short period of an individual oscillation [12]. There are two major methods of dynamic operation: amplitude-modulation (AM-AFM) and frequency-modulation (FM-AFM) operation. AM-AFM uses changes in the amplitude as feedback, while FM-AFM uses changes in the phase.

1.2 Multifrequency AFM

In traditional AFM, due to the nonlinear motion of the cantilever, information about the atomic processes that is encoded in the deflection at frequencies other than the excitation frequency is irreversibly lost. Neglecting these frequencies also restricts the number of visualization channels [10]. Improving spatial resolution, data acquisition times, and material properties imaging are perennial goals in AFM. At present, the most promising approaches to reach these goals involve the simultaneous excitation and the detection of several frequencies of the tip's oscillation. These frequencies are usually associated with either the higher harmonics of the oscillation or

the eigenmodes of the cantilever. The diversity of multifrequency approaches, the use of novel excitation or detection schemes, and the emphasis placed on mixing several frequencies configure a new subfield in force microscopy termed multifrequency AFM (MF-AFM) [23].

Figure 1.2 compares MF-AFM operation with that of static and dynamic AFM, showing how large amplitude oscillations excite higher eigenfrequencies. As the tip is brought sufficiently close to the sample, the amplitudes, and phases of the externally excited frequencies couple, thus providing enhanced sensitivity to the sample's properties even with gentle interactions. MF-AFM provides several new information channels owing to the numerous spectral components created, many of which can be mapped back into local surface properties [26].

1.2.1 Applications

Multifrequency AFM methods have been used in a variety of fields, from energy storage to nanomedicine, and can investigate properties that are as accessible with conventional AFM methods. Garcia and Herruzo [10] identify 4 key application areas:

1. **Mapping protein flexibility with molecular resolution.** Protein flexibility plays a central role in binding to other proteins either isolated or embedded in a membrane as cell receptors. Current methods for the determination of the protein flexibility give results on a timescale of picoseconds that might not be relevant to the speed at which proteins undergo conformational changes in physiological conditions (micro- to milliseconds). Multifrequency AFM methods have measured, with molecular resolution, the flexibility of several proteins in liquid.
2. **Imaging the mechanical vibrations of carbon-based resonators.** Carbon nanotubes and graphene sheets have been used to fabricate mechanical resonators that can be operated at ultrahigh frequencies, have tunable resonance frequencies, and can be used as ultra-sensitive inertial mass sensors. A Multifrequency AFM approach has been implemented to detect, identify and image the spatial shape of the eigenmodes of these resonators. This method has enabled the observation of a new class of exotic nanoscale vibration eigenmodes not predicted by earlier theories.
3. **Mapping ion diffusion.** Lithium-ion batteries are common in applications such as mobile electronic devices and electric and hybrid vehicles. The movement of lithium ions into and out of electrodes is central to the operation of those batteries. However, this displacement has not been described at the nanoscale, and this limits the understanding of the mechanisms underpinning lithium-ion battery operation. Multifrequency AFM experiments have demonstrated the existence of a strong coupling between lithium-ion concentration and cathode lattice parameters. They have established that the diffusion coefficient increases for certain grain orientations and single-grain boundaries. The sensitivity of the experiments enabled measurement of the changes in the lattice parameter associated with the ion

diffusion and migration. The results offer a direct path to improving the electrochemical performance of lithium-ion batteries.

4. **Subsurface imaging in cells.** Imaging structures beneath the surface of a sample with sub-100 nm spatial resolution has been a significant challenge in microscopy since antiquity. Multifrequency AFM has demonstrated its potential for the non-destructive imaging of embedded or buried substructures of several animal and plant cells. Experiments have been performed without any labelling or sectioning of cells, and under physiologically viable conditions.

The amount of data that can now be acquired from AFM has become sufficiently large that invoking big, deep and smart data approaches seems a necessary solution. Santos et. al. [24] have proposed turning the data from force AFM maps into abstract machine learning features to exploit standard machine learning algorithms for assistance in the identification of materials. Through standardization of the data and its transformation into abstract features more familiar to the machine learning community, built-in standard libraries in common programming languages such as Python, Matlab and R will become immediately available and catalyze translational research from materials science to computational scientists.

1.3 Objectives

Given the novelty of MF-AFM and its reliance on feedback control, it seems prudent to investigate its response to some of the principal control methods in traditional AFM. The aim of this project is do just that. It will start by developing a model of the MF-AFM system based on existing literature, as well as a model for the controller, and continue to simulating the system and studying its solutions.

The rest of the paper is structured as follows: Chapter 2 provides a literature review of AFM, its components and functionality, as well as an overview of the origin of MF-AFM and current control techniques. Chapter 3 develops the mathematical and computational models that will be used in the project. Chapter 4 describes the execution of the simulations and analyzes the results of the experiments. The paper concludes with chapter 5 and a short discussion on the current direction and issues facing the field.

LITERATURE REVIEW

2.1 Mathematical Models

In modelling the system dynamics of AFMs, most papers use interatomic potentials, nanoscale contact mechanics, or coefficient of restitution (COR) models of impact to describe the cantilever-sample system [5, 11].

2.1.1 Cantilever

The cantilever properties of interest in dynamic AFM are the force constant (or spring constant or stiffness), k , the resonant frequency, ω , and the quality factor, Q . The force constant enables transformation of intermolecular and nanoscale forces into force measurements. The resonant frequency factors into the time response of the instrument. The quality factor is a measure of the damping of the cantilever with the environment and includes the cantilever internal energy losses [5].

There are 2 main modeling approaches for AFM cantilevers: lumped parameter modeling and distributed parameter modeling [18]. Both are shown in Figure 2.1. The lumped parameter method, commonly referred to as the point-mass spring model, consists of modeling the cantilever as a damped harmonic oscillator,

$$(2.1) \quad m \frac{d^2z}{dt^2} + \frac{m\omega_0}{Q} \frac{dz}{dt} + kz = F_{ts} + F_0 \cos \omega t$$

where m is the cantilever's mass and z is its deflection from its equilibrium position due to the tip-surface interaction forces, F_{ts} ; Q , k , and ω_0 are the quality factor, force constant, and fundamental angular resonance frequency of the free cantilever, respectively; F_0 and ω are, respectively, the amplitude and angular frequency of the driving force. The point-mass model is

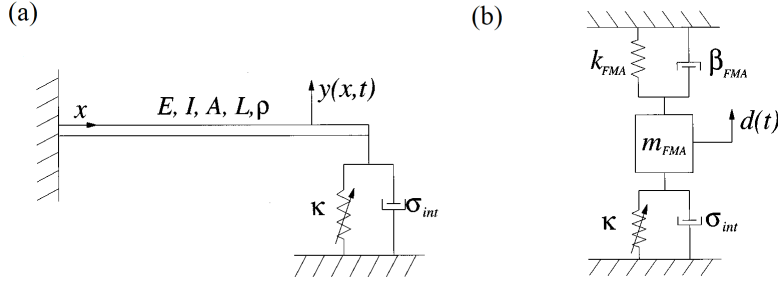


Figure 2.1: Cantilever modelled as (a) a continuous beam without the tip and (b) a damped harmonic oscillator [13][5]

generally viewed as the most straightforward approximation and is the approach taken by most published works. It is limited, however, by considering only 1 degree of freedom (DOF) and is typically incapable of modeling the higher vibration modes and possible coupling between them [10].

Distributed parameter (or continuous) modeling applies beam theory to approximate the cantilever as a rectangular beam or, in the case of V-shaped cantilevers, multiple beams. The symmetry of rectangular beams enables the derivation of a partial differential equation (PDE) for the cantilever tip system. For most cases, the result is a modified Euler-Bernoulli beam equation with the introduction of dissipative elements and tip-surface interactions

$$(2.2) \quad EI \frac{\partial^4}{\partial x^4} \left[w(x,t) + \eta_0 \frac{\partial w}{\partial t} \right] + \rho Wh \frac{\partial^2 w(x,t)}{\partial x^2} = -\eta_1 \frac{\partial w}{\partial t} + \delta(x-L) [F_e(x,t) + F_{ts}(d)].$$

Here, $w(x,t)$ is a function of displacement x along its main axis; E , ρ , and I are the Young's modulus, mass density, and area moment of inertia, respectively; L , W , and h are the length, width, and height of the cantilever, respectively; η_0 and η_1 are, respectively, the internal and external damping coefficients; F_e is the excitation force and F_{ts} represents all of the tip-sample interaction forces. The delta function, δ , localizes the tip-sample forces at the free end of the cantilever. The tip is not considered directly in this model; however, it is in determining tip-sample forces [5].

2.1.2 Tip-Sample Forces

The forces relevant to AFM are ultimately of electromagnetic origin. However, different intermolecular, surface, and macroscopic effects give rise to interactions with distinctive distance dependencies. In the absence of external fields, the dominant forces in air are van der Waals interactions, short-range repulsive interactions, adhesion, and capillary forces [12]. In liquid, the solid-liquid interface together with the presence of ions and electrolytes give rise to additional forces such as the electric double layer and the solvation forces. Some of those forces are attractive while others are repulsive. In some cases, interaction forces could show oscillations. The repulsive or attractive character of electrostatic interactions could be changed in liquid by modifying the

Geometry	Force
2 Flat Surfaces	$f = \frac{H}{6\pi d^3}$
2 Spheres	$F = -\frac{H}{6d^2} \frac{R_1 R_2}{R_1 + R_2}$
Sphere - Flat Surface	$F = -\frac{HR}{6d^2}$
Cone - Flat Surface	$F = -\frac{H \tan^2 \theta}{6d}$
Cone - Sphere	$F = -\frac{H}{6} \left[\frac{R}{d^2} + \frac{\tan^2 \theta}{d+R_\theta} - \frac{R_\theta}{d(d+R_\theta)} \right]$
Paraboloid - Flat Surface	$F = -\frac{H}{12d^2} \frac{l_{xy}}{l_z}$
Cylinder - Flat Surface	$F = -\frac{HR^2}{6d^3}$

Table 2.1: van der Waals interaction laws for most common AFM geometry (H is the Hamaker constant, d is the tip-surface distance, R is the radius of the sphere / cylinder, θ is the semi-aperture of the cone, $R_\theta = R(1-\sin\theta)$, and l is the semi-axis of the paraboloid. $H = \pi^2 C \rho_1 \rho_2$, where C is the constant in the atom-atom pair potential and ρ_1 and ρ_2 are the number of atoms per unit volume. The formula for 2 flat surfaces calculates force per unit area [9]).

ionic strength. Typically, force curves of interaction may be divided into long range and short range regions [21][5].

The long range region extends several nanometers above the sample surface. Long-range interactions of van der Waals type arise from fluctuations of the electric dipole moments of atoms and their mutual polarization. The 3 possible dipole interactions, dipole-dipole (or Keesom interaction), dipole-induced dipole (or Debye force), and induced dipole-induced dipole (or London dispersion), scale as r^{-6} , where r is the distance between atoms or molecules. Field fluctuations are universal which makes van der Waals forces ever-present, independent of the chemical composition of the surfaces or the medium. The van der Waals force between two surfaces is usually attractive. There are, however, situations where this may not be the case. For example, the van der Waals force between two different materials in liquids could be attractive or repulsive, depending on the values of the dielectric constants and the refractive indexes of the interface [8]. Van der Waals forces are amenable to several theoretical treatments of varying complexity [28]; Common approximations and their force equations are displayed in Table 2.1.

Despite the quantum mechanical nature of the short-range interaction region, if the contact area between two objects involves hundreds or thousands of atoms, repulsive forces may effectively be described by contact mechanics. Continuum elasticity theories explain the contact and adhesion between finite bodies under external load. Elastic materials are characterized by constitutive equations, which describe the functional relationship between stress and strain tensors. The general solution to these equations for an elastic material with arbitrary displacement (and frictionless contact) yields expressions from which the radius of contact a , the deformation at the contact center δ , and the magnitude of the load P can be determined.

	Hertz	DMT	JKR
a	$3 \sqrt{\frac{RP}{E_{eff}}}$	$3 \sqrt{\frac{R}{E_{eff}}(P + 2\pi rW)}$	$3 \sqrt{\frac{R}{E_{eff}}(P + 3\pi rW + \sqrt{6\pi rW + (3\pi rW)^2})}$
δ	$3 \sqrt{\frac{P^2}{RE_{eff}^2}}$	$3 \sqrt{\frac{(P+2\pi rW)^2}{RE_{eff}^2}}$	$\frac{a^2}{R} - \frac{2}{3} 3 \sqrt{\frac{6\pi W a}{E_{eff}}}$
F_{ad}	0	$2\pi rW$	$\frac{3\pi rW}{2}$

Table 2.2: Equations for contact radius a , sample deformation δ , and adhesion force F_{ad} for a spherical tip on a flat surface according to Hertz, DMT, and JKR (P is the force exerted by the tip on the surface) [18][5]

Several theories describe the elastic deformation of the sample. Differences in the relations between the applied load P and the contact radius a or the deformation δ are due to the role played by adhesion in the considered system. Table 2 summarizes the relations between the contact radius, deformation of the sample, and the adhesion force for a spherical tip on a plane surface according to the 3 most used theories: Hertz, Derjaguin-Müller-Toporov (DMT), and Johnson-Kendall-Roberts (JKR) [7]. The Hertz model neglects the effects of adhesion, whereas the other two take account of it outside (DMT) or inside (JKR) the contact area. Thus, Hertz theory is applicable only when the adhesion forces are negligible compared to the applied load. DMT theory is typically used in the case of small tips and stiff samples with a small adhesion, whereas JKR is applied for large tips, soft samples, with large adhesion. All of the theories, however, assume smooth surfaces with no plastic deformation and no viscoelastic phenomena [5, 9] [5].

2.2 Nonlinear Dynamics

The tip surface forces relevant to dynamic AFM have a nonlinear dependence on distance. Cantilevers possess several distinct eigenmodes and the amplitudes of interest range from 1 – 30 nm, which is longer than the decay length of said forces. Thus, the cantilever tip experiences nonlinear forces which, for the most part, cannot be linearized. Accordingly, the cantilever may vibrate in interesting and unexpected ways; some may be detrimental to imaging stability while others can be exploited to enhance performance. Understanding these phenomena can offer greater insight into the physics of dynamic AFM and provide new opportunities for achieving improved material contrast with gentle imaging forces [15]. A deeper understanding of cantilever dynamics is becoming increasingly important in 2 of the biggest growth areas: (i) the manipulation and imaging of soft matter and (ii) the accurate characterization of sample properties in material science [19].

Dynamic AFM attempts to drive the microcantilever externally into a resonance of a specific eigenmode. The main eigenmodes consists of bending modes (denoted B_1, B_2 , etc.) transverse to the plane of the cantilever and torsion modes (denoted T_1, T_2 , etc.) where the B_n or T_n mode

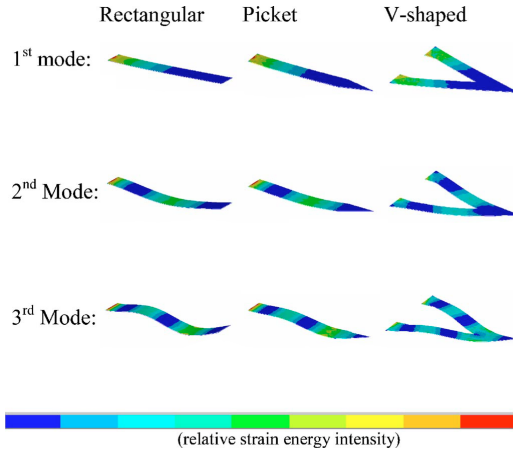


Figure 2.2: 1st 3 bending modes for rectangular-, picket-, and V-shaped cantilevers and strain energy density contour. Reproduced from [5].

$(n = 1, 2, \dots)$ contains $n-1$ vibration nodes along the axis of the cantilever. Occasionally the lateral bending modes $L1, L2$, etc. can also be observed when the cantilever bends in its plane laterally. The greater the mode number, the larger the resonance frequency and Q-factor and the greater its spatial modulation. When a cantilever eigenmode is excited by tuning the drive frequency to the eigenmode's natural frequency, the tip motion should oscillate harmonically with a well-defined motion. If a bending mode Bn is excited, ideally the tip should oscillate perpendicular to the surface, while if one of the torsion modes Tn is excited, the tip should oscillate tangentially to the sample surface. Some eigenmodes, however, couple torsional and bending motions or torsional and lateral motions. Such coupled modes are denoted as bending-torsional (BT) or lateral-torsional (LT) modes. If such nodes are excited, the tip moves both tangentially and normally to the sample surface [14]. Figure 2.2 displays the 1st 3 eigenmodes for a rectangular-, picket-, and V-shaped cantilever, as well as their strain gradients.

2.3 Control Techniques

One of the characteristic and interesting features about AFM is that imaging depends entirely on a feedback control loop [1]. The most common control approaches use piezo-electric actuators, optical detection of cantilever deflection, and PI or PID control. As mentioned in Section 1.2, AFMs can operate in a variety of modes, including contact mode (where the control loop tries to maintain constant contact force with the sample surface) and dynamic modes (where the control loop tries to maintain a constant oscillation amplitude as the tip periodically comes into contact with the sample surface). The nonlinearity of the interaction force, as shown in Figure 3.1 b, shows why feedback operation for tracking the sample topography is crucial for obtaining reliable data about the sample surface.

The piezo actuator is usually modeled as a second-order resonance, leading to a lack of

integrators in the forward path. This necessitates the use of integral action for zero steady-state error to any steps in the surface height. The addition of a second integrator via PII control can provide zero steady-state error to surface slopes, which are common in many samples [23]. Such controllers are necessarily low bandwidth, however, since the lack of phase lead means that the gain must be rolled off below the resonance of the actuator.

The typical industrial AFM control loop, whether done in contact or dynamic mode, is a low frequency PI or PII loop. A general form of an analog controller that admits PI, PD, PID, PII, and even PIID is:

$$(2.3) \quad C(s) = \left(K_p + \frac{K_i}{s} + \frac{K_{ii}}{s^2} + K_d s \right) E(s),$$

where $E(s)$ is the Laplace Transform of the error signal $e(t)$. For a P, PI, PII, or PID controller, one or more of the gains K_d , K_i , or K_{ii} are set to zero.

Most of the issues affecting AFM today are related to control problems. The main ones include ease of use, instrument calibration, and process speed [1]. These issues largely arise from the characteristics of the piezo actuators used in the AFM, which makes reliable modeling of the actuator more difficult.

2.4 Bimodal AFM

There are multiple approaches to MF-AFM that are widely used. One of the first and most commonly used is Bimodal AFM, where two driving forces are used to excite the vibration of the cantilever. The excitation frequencies are tuned to match two of the flexural eigenmodes of the cantilever, usually the first and the second bending modes. An output signal of the first mode (either the amplitude or the frequency shift) is used to image the topography of the surface while the output signals of the second mode (amplitude and/or phase shift) are used to measure changes in mechanical, magnetic, or electrical properties of the surface. This method is compatible with both dynamic AFM modes and can be performed in air, liquid, or ultrahigh vacuum. Bimodal AFM offers a straightforward approach to separate topography from other interactions influencing the tip motion such as magnetic or electrostatic forces. Thus, the different resonances of the cantilever could be channels to access and separate different sample properties [5, 10].

The dynamics of the modes are coupled via the non-linear tip-sample force F_{ts} [23]. The absolute position z is the sum of the two modes taken into account in the modal approximation $z \approx z_1 + z_2$ or frequencies

$$(2.4) \quad z_{(m)} \approx z_{(m)0} + \sum_{n>0}^N A_{(m)n} \sin(n\omega t + \phi_{(m)n}),$$

where $m = 1, 2$ is the mode number and n is the harmonic number. $z_{(m)0}$ is the mean deflection of mode m , $A_{(m)n}$ and $\phi_{(m)n}$ are its amplitude and phase shift, respectively. The approximation

implies that N is finite. The net energy entering ($E_{T(m)} < 0$) or leaving ($E_{T(m)} > 0$) a given cantilever mode m can then be written as

$$(2.5) \quad E_{T(m)} = - \oint F_{ts} \cdot \dot{z}_m dt,$$

where \dot{z}_m is the time derivative of z_m . $E_{T(m)}$ is the net energy transfer per cycle via mode m , and does not take into account losses due to a viscous medium.

PROJECT MODEL

3.1 Single Mode

For normal (single mode) AFM operation, the cantilever was modeled as a mechanical point mass impact oscillator, in accordance with [4]. The hybrid dynamical system is given in state-space form as

$$(3.1) \quad \begin{cases} \dot{x}_1 = x_2 \\ \dot{x}_2 = -\omega_n^2 x_1 - \frac{\omega_n}{Q} x_2 + u + F(b + x_1 - \sigma) \end{cases}$$

when the tip is away from the sample, together with the reset law

$$(3.2) \quad x_1(t^+) = x_1(t^-), \quad x_2(t^+) = -rx_2(t^-)$$

that models the impact between the cantilever tip and the sample surface (in terms of a change in state in the infinitesimally short time before and after an impact, at times t^- and t^+ , respectively). In (3.1) – (3.2)

- x_1 is the vertical position of the tip with respect to b ;
- x_2 is its vertical velocity;
- $\omega_1 = \sqrt{\frac{k}{m}}$ is the natural (or resonant) frequency of the 1st flexural mode of the cantilever, with m and k being the mass and force constant of the cantilever, respectively;
- Q is the quality factor;

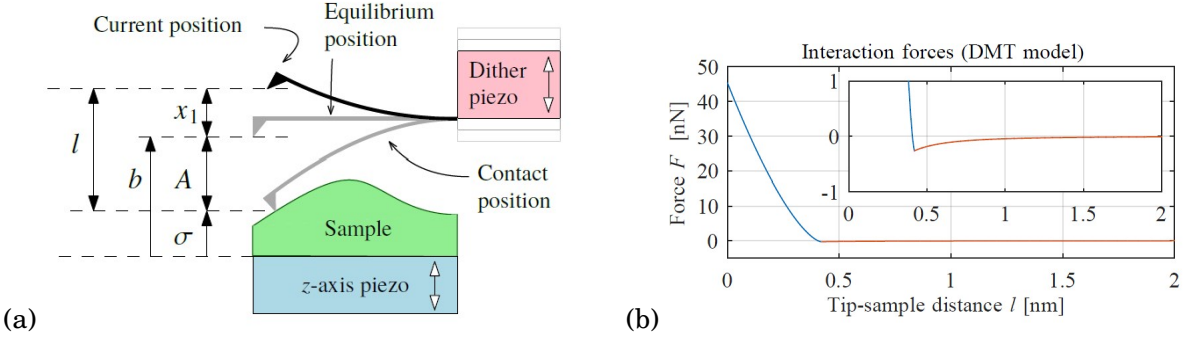


Figure 3.1: AFM Model: (a) Schematic of the cantilever tip close to the sample surface. (b) Interaction forces according to Derjaguin-Muller-Toporov model (DMT), with coefficient values in Table I. The inset shows the detail of the repulsive forces. Reproduced from [4]

- $u = D \sin(\omega_d t)$ represents the action of the dither piezo, with D being its driving amplitude and ω_d its driving frequency. D is calculated using the formula

$$(3.3) \quad D = A_f \left| \omega_1^2 - \omega_d^2 + \frac{\omega_n}{Q} i \omega_d \right|,$$

where A_f is the free oscillation amplitude and $i = \sqrt{-1}$;

- F is the interaction force normalized to mass depending on the distance of l between the tip and the sample, where $l = b + x_1 - \sigma$;
- b is the height of the base of the cantilever
- σ is the height of the sample surface to be measured;
- r is the restitution coefficient.

With respect to the interaction force, F in Equation (3.2), the Derjaguin-Muller-Toporov model (DMT) is used, where the system is modeled as a spherical tip coming to contact with a locally flat sample surface. As such

$$(3.4) \quad F(l) = \begin{cases} -\frac{H r_t}{6 l^2} & l > l_m \\ -\frac{H r_t}{6 l_m^2} + \frac{4}{3} \frac{\sqrt{r_t (l_m - l)^3}}{\frac{1 - V_t^2}{E_t} + \frac{1 - V_s^2}{E_s}} & l \leq l_m \end{cases}$$

with:

- l being the tip-sample distance;
- H the Hamaker constant;
- r_t the tip radius;

- l_m the intermolecular distance;
- E_t and E_s the elastic moduli of the tip and the sample, respectively;
- V_t and V_s the Poisson ratios of the tip and the sample, respectively.

When the tip and the sample are not too close, a small residual attraction exists between them. Conversely, when the tip-sample distance is reduced below the intermolecular distance l_m , repulsive forces dominate and the overall repulsive force becomes larger as l decreases [4]. A depiction of the AFM system, as well as a graph of the DMT force curve, are shown in Figure 3.1.

3.2 Multifrequency

The multifrequency AFM dynamics were modeled based on the theory developed by [16], which explains the origins of the high force sensitivity observed in experiments. The Euler-Bernoulli PDE of Eq. 2.2 is approximated by a system of n 2nd-order ordinary differential equations (ODE), one for each eigenmode of the cantilever. It is assumed that the dynamics of the system is mostly contained in the lower eigenmodes. A system of two differential equations is then obtained as

$$(3.5) \quad \begin{cases} m\ddot{z}_1 = -k_1 z_1 - \frac{m\omega_1}{Q_1} \dot{z}_1 + D_1 \cos \omega_1 t + D_2 \cos \omega_2 t + F_{ts}(z_1 + z_2), \\ m\ddot{z}_2 = -k_2 z_2 - \frac{m\omega_2}{Q_2} \dot{z}_2 + D_1 \cos \omega_1 t + D_2 \cos \omega_2 t + F_{ts}(z_1 + z_2), \end{cases}$$

where Q_i , k_i , $\omega_i = 2\pi f_i$, and $D_i = \frac{k_i A_{0i}}{Q_i}$, are, respectively, the quality factor, force constant, angular frequency, and external excitation force of the i eigenmode, with A_{0i} being the free amplitude. m is again the effective mass of the cantilever.

By making the substitutions $y_1 = z_1$, $y_2 = \dot{z}_1$, $y_3 = z_2$ and $y_4 = \dot{z}_2$, Eq 3.5 can further be deconstructed into the following system of 1st-order ODEs that can be solved with standard numerical integration:

$$(3.6) \quad \begin{cases} \dot{y}_1 = y_2, \\ \dot{y}_2 = -\frac{k_1}{m} y_1 - \frac{\omega_1}{Q_1} y_2 + \frac{D_1}{m} \cos \omega_1 t + \frac{D_2}{m} \cos \omega_2 t + F(b + (x_1 + x_3) - \sigma), \\ \dot{y}_3 = y_4, \\ \dot{y}_4 = -\frac{k_2}{m} y_3 - \frac{\omega_2}{Q_2} y_4 + \frac{D_1}{m} \cos \omega_1 t + \frac{D_2}{m} \cos \omega_2 t + F(b + (x_1 + x_3) - \sigma), \end{cases}$$

where y_1 and y_3 are the displacements, and y_2 and y_4 are the velocities, of the 1st and 2nd eigenmodes, respectively. $F_{ts} = F(b + (x_1 + x_3) - \sigma)$ are the tip sample interactions, again based on the DMT model defined in Eq. 3.4.

3.3 Control Strategy

Synthesizing a controller and proving its validity analytically is not trivial. PID control is a well-established solution to the problem of controlling the cantilever base height in AFM experiments,

however it has not yet been studied extensively in the multifrequency regime. For this reason, we chose to focus on the response of MFAFM to PID control.

Ideally, the reset law Eq. 3.2 is triggered once every oscillation period when the tip impacts the sample surface. As a result, under normal working conditions with only low velocity impacts, the evolution of the tip position in time follows a quasi-sinusoidal motion that can be approximated as

$$(3.7) \quad x_1(t) \approx A(t) \sin(\omega_d t + \phi(t))$$

with

$$(3.8) \quad A(t) \approx b(t) - \sigma(t)$$

It is this amplitude, estimated as the difference between the base height and the sample height, that is then used as the feedback signal in the control loop.

For correct operation, the oscillation amplitude A should attain a certain constant reference value A_r , i.e.

$$(3.9) \quad \lim_{t \rightarrow \infty} A(t) = A_r$$

This regulation is fundamental. If A becomes too small, the interaction forces and the velocity of the cantilever tip could damage the sample. If A becomes too large, the oscillating cantilever tip risks loosing contact with the sample, causing the undesirable phenomenon known as *probe loss*, in which, after the sample surface has decreased rapidly, the cantilever oscillates freely leading to erroneous measurements.

To ensure (3.8), the PID controller is applied to the z -axis piezo to adjust the base height b . The PID control law is expressed by

$$(3.10) \quad b(t) = PID(e_A)$$

where $e_A = A_r - A(t)$ is the error on the oscillation amplitude and the PID control action is classically defined as

$$(3.11) \quad PID(\zeta(t)) = K_P \zeta(t) + K_I \int_0^t \zeta(t) d\tau + K_D \frac{d\zeta(t)}{dt}$$

where K_P , K_I , and K_D are the proportional, integral, and derivative gains, respectively. Traditionally, $A_r \approx 0.9A_f$, where A_f is the free oscillation amplitude, i.e., the amplitude the cantilever would oscillate at without the influence of interaction forces [4].

RESULTS

4.1 Calculations

By choosing values for the initial state of the cantilever's eigenmode(s), the set of ODEs in Equation 3.1 may be turned into an initial value problem (IVP) for single mode operation. Using the initial condition, x_0 , as well as a period of time over which the answer is to be obtained, (t_0, t_f) , the solution is obtained iteratively using an ODE solver installed within the numerical computing environment MATLAB®. At each step the solver applies a particular algorithm to the results of previous steps [25]. At the first such step, the initial condition provides the necessary information that allows the integration to proceed. The final result is that the ODE solver returns a vector of time steps $t = [t_0, t_1, t_2, \dots, t_f]$ as well as the corresponding solution at each step $x = [x_0, x_1, x_2, \dots, x_f]$. For bimodal simulations, an initial state, y_0 , for each of the eigenmodes position (y_1 for the first mode, y_3 for the second mode) is used to turn Equation 3.6 into an initial displacement and velocity for each state, along with a similarly defined time period.

To implement PID control in the time domain numerically, the ODE solver can be utilized to integrate the error signal, similar to the approach described in [27]. By creating an extra state defined as the error, the solutions of this state can then be multiplied by the integral gain constant to form the intergral portion of the PID control. In other words, adding states $x_3 = y_5 = A_r - A$ to Equations 3.1 and 3.6, respectively, where A_r is the reference amplitude and A is the estimated amplitude defined by Equation 3.8, can then lead to the control law 3.10 being defined as

$$(4.1) \quad b = PID(e_A) = K_P(A_r - A) + K_I(x_3 | y_5) + K_D(\dot{e}_A(t))$$

where $\dot{e}_A(t)$ is calculated as the numerical gradient of a growing vector of error values $e_A(t)$.

The ODEs of Equations 3.1 and 3.6 are of explicit form $\dot{y} = f(t, y)$, where the first derivative can be written directly as a function of the other states and time. However, with the addition of the

error term as a state-space equation in the monomodal and bimodal simulations, the equations also exhibit a difference in scaling. Due to the difference in time scales between the error signal and the other solution components, the equations can become stiff. For this reason, the ODE solver *ode15s* for the two experiments. Table 4.1 displays the values used for the cantilever characteristic parameters of the 1st flexural eigenmode. The free amplitudes varied with the sample being estimated.

The AFM models of Section 3.1 and 3.2, along with the control approach described in Section 3.3, were tested against three calibration surfaces: a flat surface, a square-wave surface, and a ramped surface. To test the accuracy of the model, each sample was graphed and the trajectory of the cantilever simulated initially without any control applied to the base in monomodal operation. The results are shown in Figures 4.1 - 4.3. For each run, the input signal u had a sample time $t_s = 10^{-9}$ s, duration of $t_T = 10^{-4}$ s, and an angular drive frequency $\omega_d = 2\pi \times 10^5$, which is close to the first resonant frequency ω_n calculated using the parameters in Table 4.1. The drive amplitude, D was calculated using Equation 3.3, with the free oscillation amplitude $A_f = 50$ nm in each test.

The cantilever simulation began from an initial tip position of $A_r = 0.9A_f$, which is also the value of the base b as defined in 3.1a. The red circles seen within the graphs of the trajectory are event markers that indicate each time the cantilever tip has made physical contact with the sample, defined at the point when $l = b + x_1 - \sigma = 0$. As can be seen in Figure 4.1, the cantilever

Group	Parameter	Value
Cantilever	m	1.3098×10^{-11} kg
	c	2.3455×10^{-7} kg/s
	r	0.9
	k_1	42 N/m
	ω_1	$\sqrt{\frac{k_1}{m}}$ rad/s
	Q_1	$\frac{k_1}{\omega_1^2}$
Interaction forces	H	1.4×10^{-19} J
	r_t	2 nm
	l_m	0.42 nm
	E_t, E_s	1.65×10^{11} Pa
	V_t, V_s	0.27

Table 4.1: Parameters used for the AFM simulations, in accordance with [4]

	Mode 1	Mode 2
k_i [N/m]	0.9	35.2
Q_i	255	1000
f_i [kHz]	48.913	306.194
ω_i [rad/s]	$2\pi f_1$	$2\pi f_2$

Table 4.2: Parameters for Bimodal Simulations

reverses direction each time it hits the sample, in accordance with Equation 3.2. In this case, the sample height is 6 nm, and the cantilever appropriately recoils at a depth of $b - \sigma = 39$ nm below the cantilever's equilibrium position. Similar justifications can be made for the trajectories on the ramp (whose height ranges from 1 - 375 nm) and square-wave (oscillates between heights of 5 - 15 nm) samples. The model is validated.

A manual variation of the Ziegler–Nichols (ZG) method [30] was taken to tune the PID controller applied to the adjustment of the base height. The following steps are summarized as follows:

1. Begin with all gains $K_P, K_I, K_D = 0$.
2. Increase K_P until the response to a disturbance is steady oscillation.
3. Set K_P to approximately half the value obtained in the previous step to achieve "quarter amplitude decay" type response.
4. Increase K_I until any offset is corrected in sufficient time.
5. Increase K_D (if necessary) until the loop is acceptably quick to reach its reference after a load disturbance.

With this approach, the gains were found to be $K_P = 0.5$, $K_I = 8.5$, and $K_D = 0$ to sufficiently bring the error signal $e_A = A_r - (b - \sigma)$ down to zero when tested on the flat sample. When the system was tested with the same gains on the other sample surfaces, the results were not the same. The error response with these gains for all three surfaces is shown in Figure 4.4.

A similar approach is taken with bimodal operation. The cantilever's trajectory is solved without PID control applied to the base. The solutions to the first and second modes for the three calibration surfaces are shown in Figures 4.5 – 4.6. In each case the parameters were chosen in accordance with [16] and are given in Table 4.2. Applying the PID control and retaining the gains found from single frequency operation, the solutions are now those presented in Figure 4.7. Based on the error signal, the current gain settings appear to be a decent starting point and not too far from the optimal values. However, without changing K_P or K_P (as altering either increased oscillations), it wasn't until the K_I was increased from 8.5 to 250 that any noticeable

change in the error was observed, which did not include declining to zero. The results of this simulation are shown in Figure 4.8.

4.2 Analysis

In Figure 4.4, for the the ramp and square-wave samples, the error responds linearly with time, albeit in different directions. In the case of the the ramp surface, the error continues to rise as the cantilever travels up the ramp. This could be attributed to the steady decrease in the estimated amplitude A (Equation 3.8) as the sample height grows, and the inability of the controller to respond as quickly, as shown in Figure 4.9a. For the case of the square-wave surface, Figure 4.9b shows that the cantilever touches the sample only once in the duration of the input at $\sim 5 \mu\text{s}$, before oscillating freely. Further inspection showed that after this initial impact, b was then immediately set to a height 135 nm, effectively causing the system to lose proximity with the sample and explaining the increase in absolute error. By decreasing K_I to 3.5, the offset was able to be centered around zero, as shown in Figure 4.10. Further decrease in K_I saw the offset increase slightly above zero, however a pattern more closely resembling that of the surface emerges. This is shown in Figure 4.11. For the ramp surface, increasing K_I to 75 saw the error signal stop rising continuously, and level off at an offset ~ -1.5 . Additional attempts to bring the offset to zero resulted in the error either rising again or oscillating chaotically. From the bimodal simulations without PID control shown in Figure 4.5, immediately noticeable is the poor performance of the system with the square-wave sample. It did not map the line topology as well as it did for the flat and ramp surface, and appeared to miss all the 15 nm peaks while instead only touching the lower 5 nm surface. Also of note is the size of the response amplitude, $\sim 8 - 9$ nm, relative to the peaks. It is not unreasonable to expect specimen to have depths of ≥ 15 nm, further highlighting the need for an adjustment in the base height.

A possible explanation for the lack of error control may lie in the nature of operation. As mentioned in 2.4, in bimodal AFM, the absolute displacement of the cantilever is the sum of the two modes taken into account, via Equation 2.4. However, the higher mode is also operating at a higher frequency and is possibly too fast for the controller to see effectively. Because the controller is working at the fundamental frequency, higher modes may have to wait longer to experience the control affect. Initial conditions may also affect the balance of energy between the different modes and place more in the higher modes. S. Santos [23] identifies the main mechanisms of the net energy transfer defined by Equation 2.5 as the energy lost in the tip sample junction from mode m and the inter-modal energy transfer between modes. Finally, there also appears to be a time delay between the output of the control function and the numerical integrator.

4.2. ANALYSIS

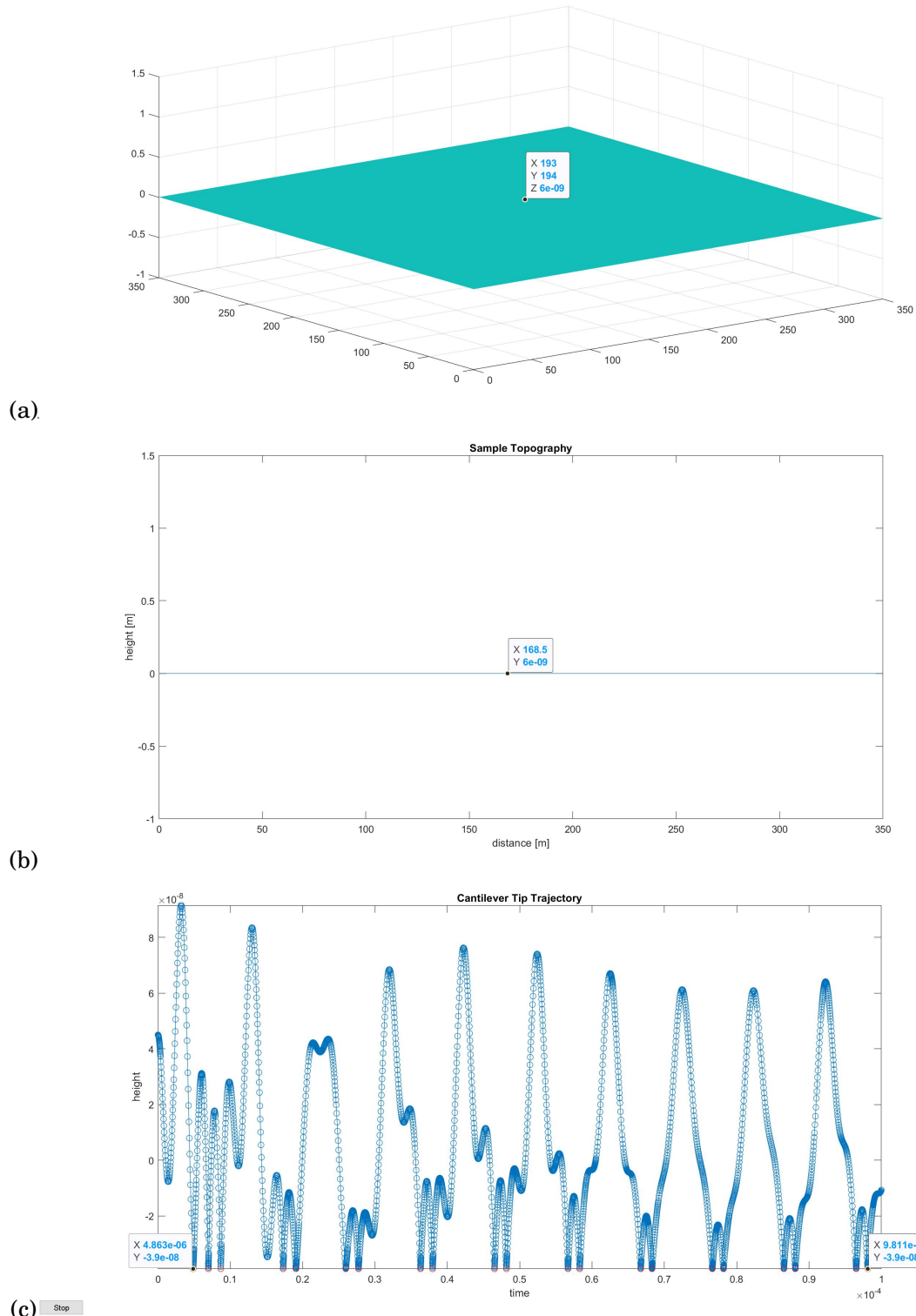


Figure 4.1: Model Validation (flat surface): (a) 3-D and (b) 2-D topographical plots of the sample. (c) Cantilever trajectory

CHAPTER 4. RESULTS

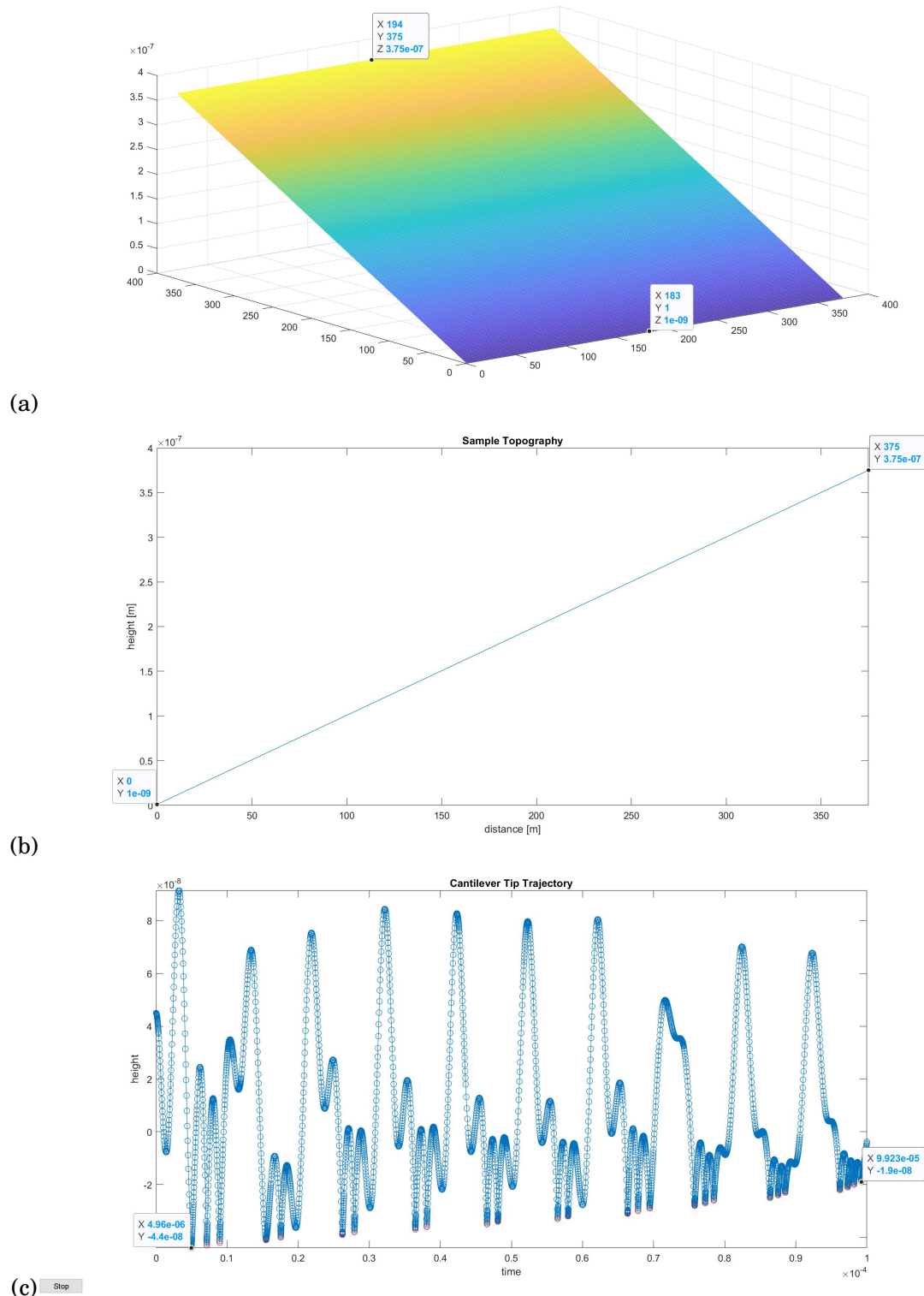


Figure 4.2: Model Validation (ramp surface): (a) 3-D and (b) 2-D topographical plots of the sample. (c) Cantilever trajectory

4.2. ANALYSIS

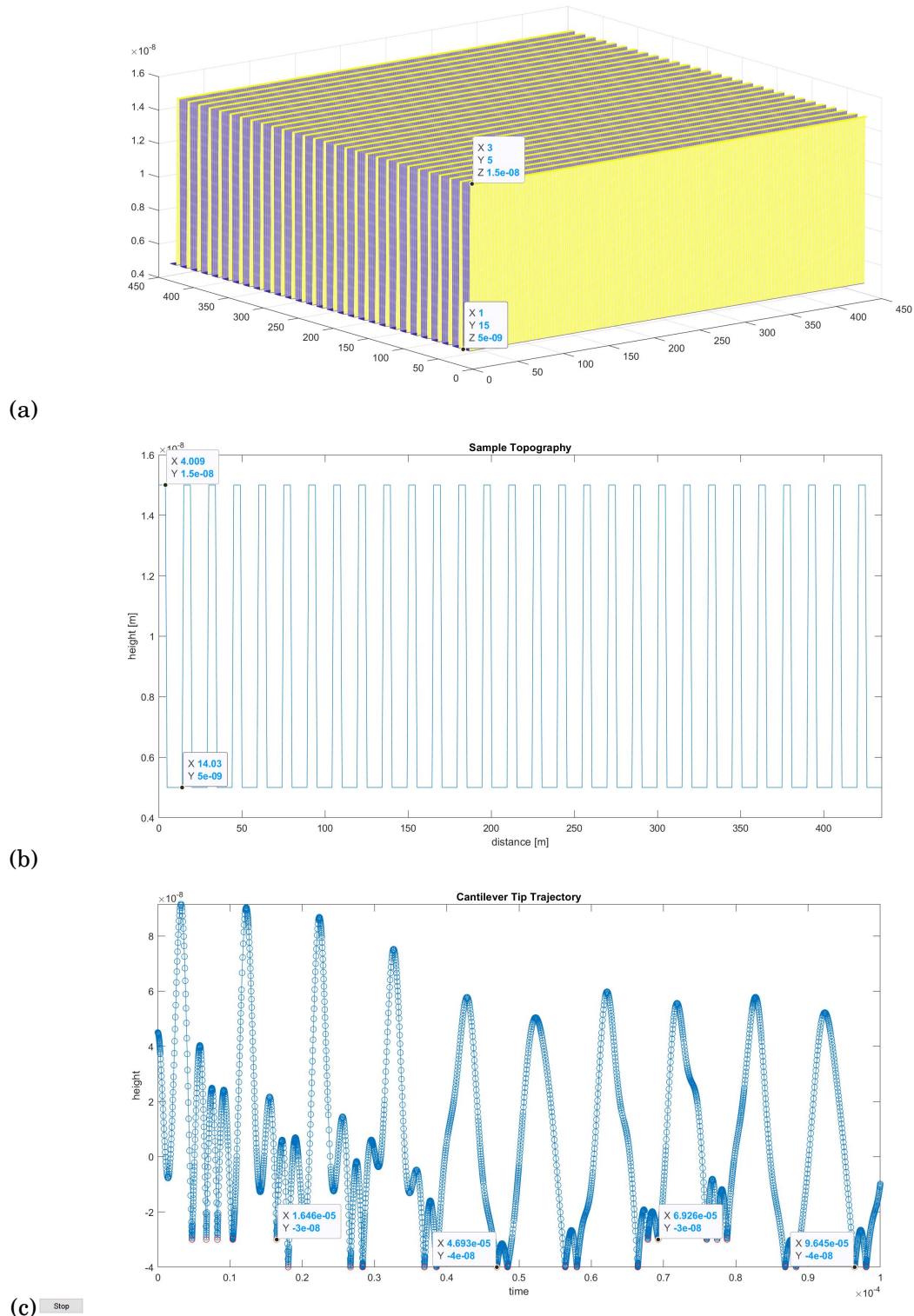


Figure 4.3: Model Validation (square-wave surface): (a) 3-D and (b) 2-D topographical plots of the sample. (c) Cantilever trajectory

CHAPTER 4. RESULTS

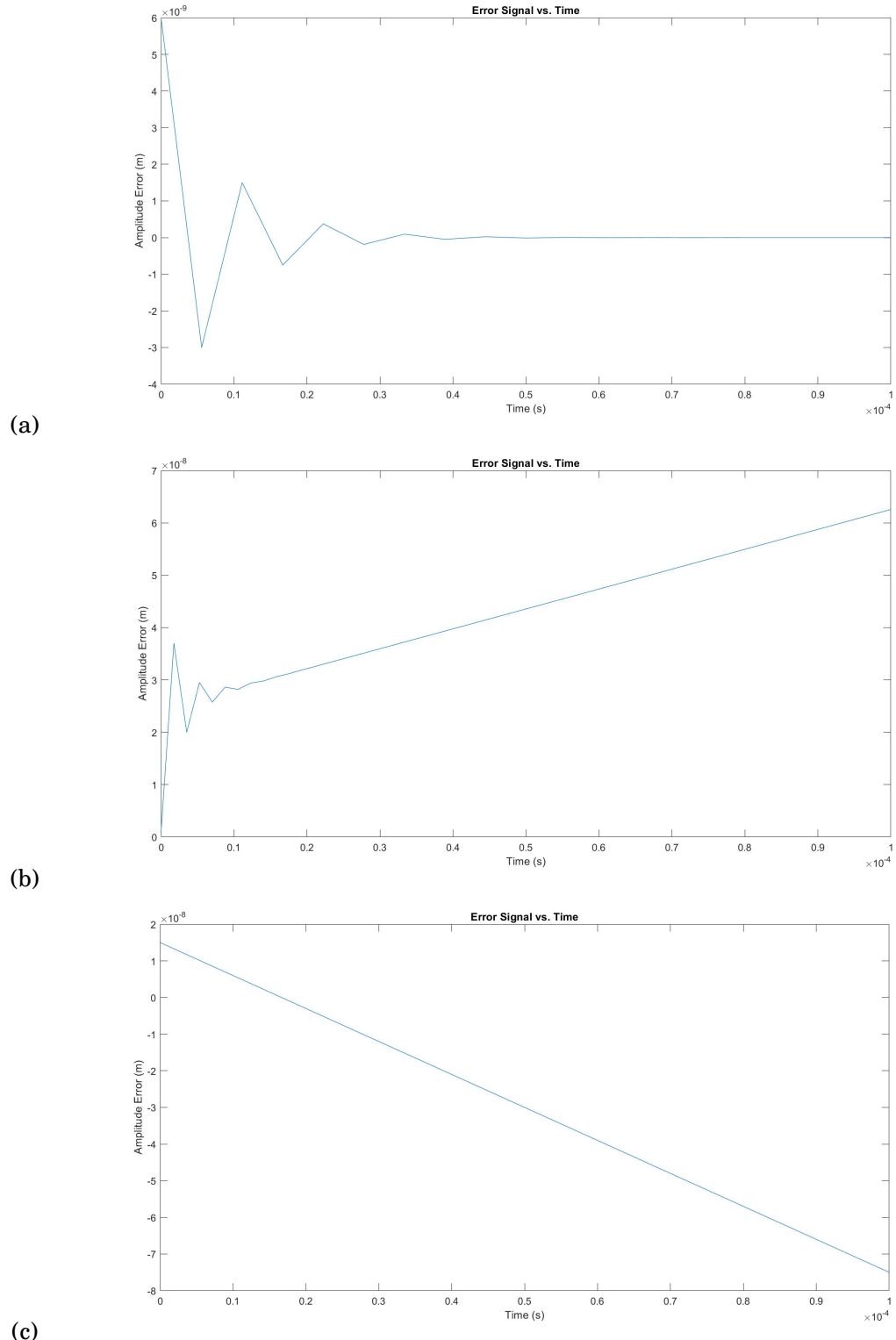


Figure 4.4: Error response $e_A \approx A_r - A$ with PID gains $K_P = 0.5, K_I = 8.5, K_D = 0$ on the (a) flat surface (4.1b), (b) ramp surface (4.2b), and (c) square-wave surface (4.3b)

4.2. ANALYSIS

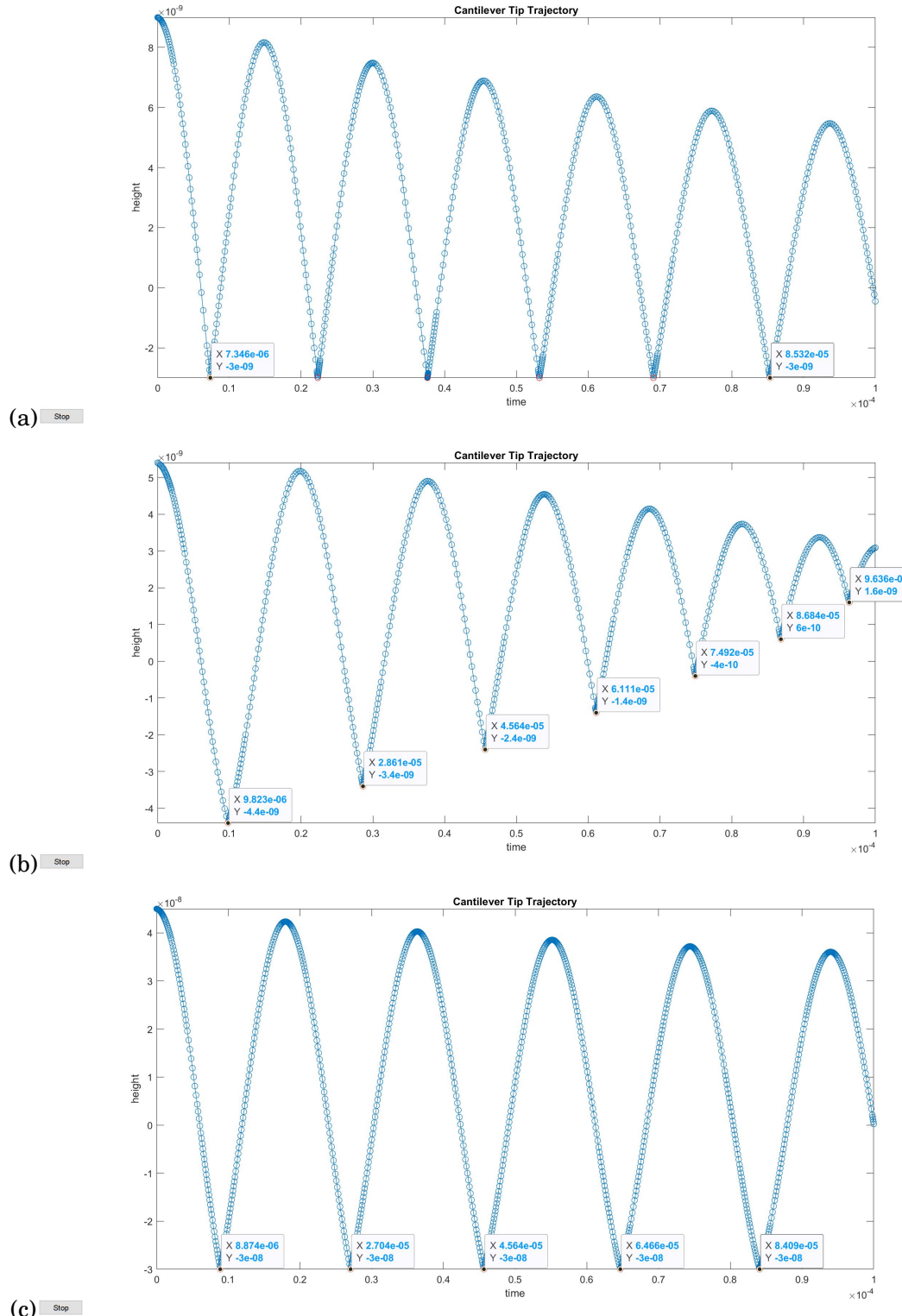


Figure 4.5: Bimodal cantilever solutions of the first flexural mode with stationary base for the (a) flat surface, (b) ramp surface, and (c) square-wave surface.

CHAPTER 4. RESULTS

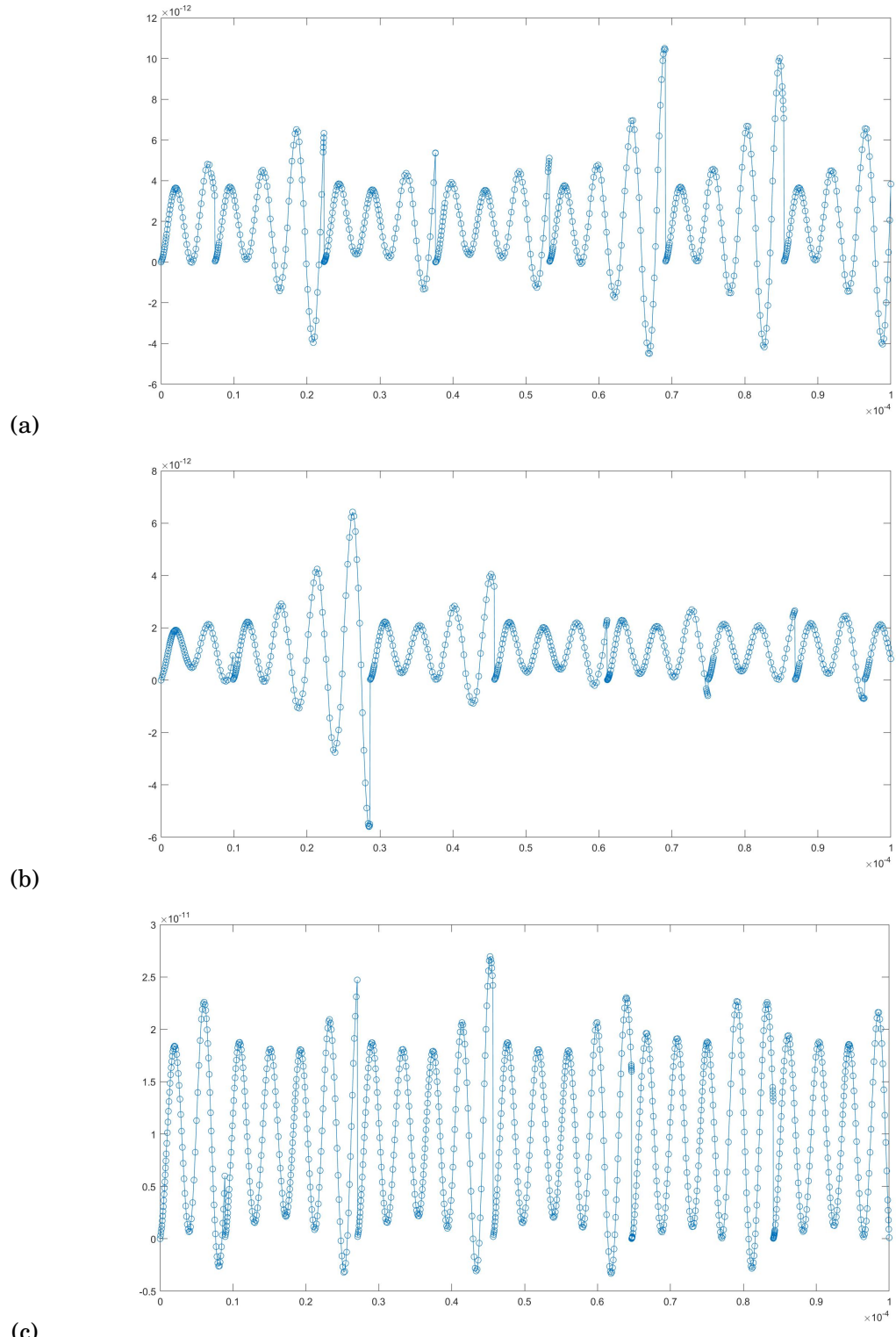


Figure 4.6: Bimodal cantilever solutions of the second flexural mode with stationary base for the (a) flat surface, (b) ramp surface, and (c) square-wave surface.

4.2. ANALYSIS

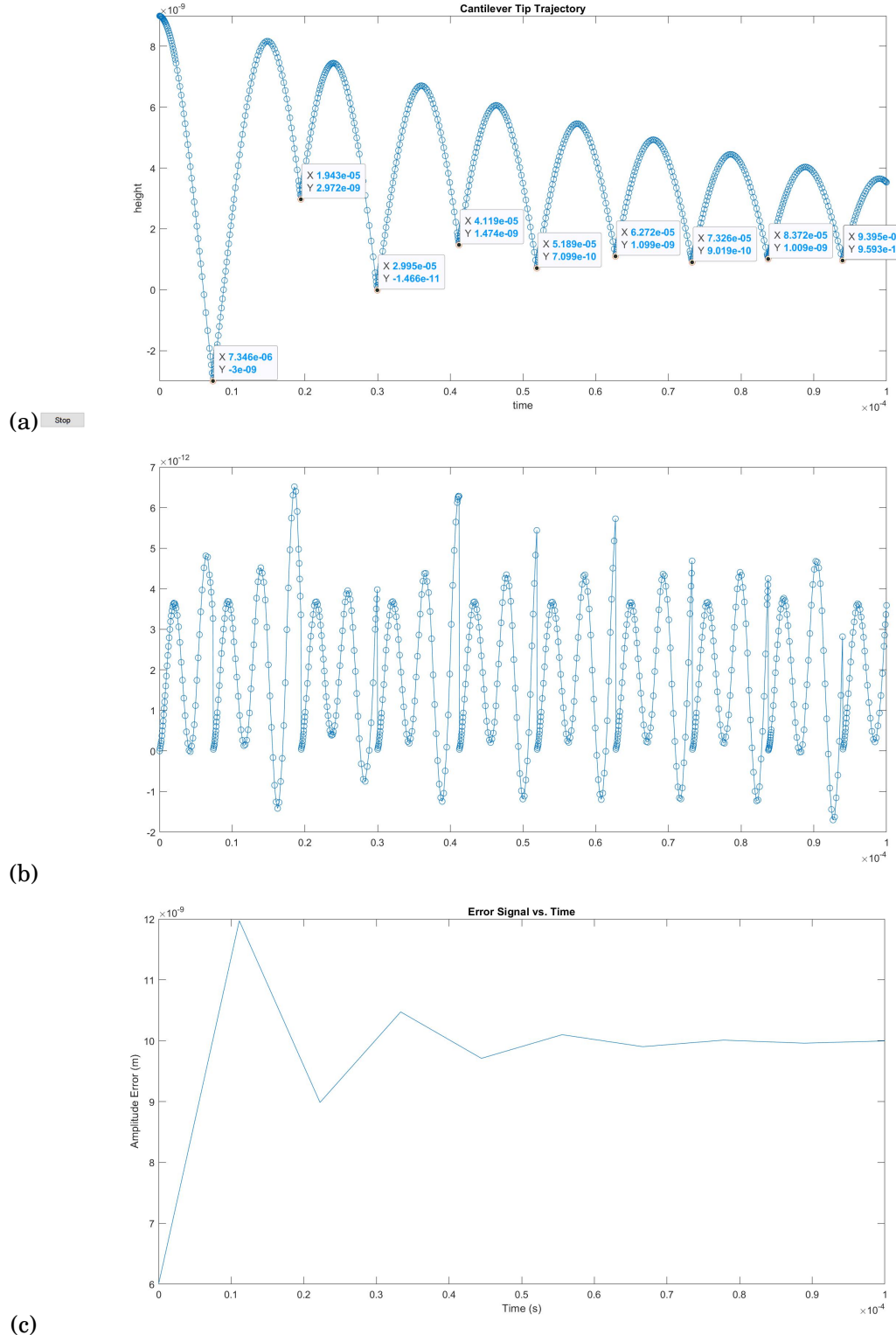


Figure 4.7: Bimodal response of (a) the first mode and (b) the second mode to PID control with gains $K_P = 0.5$, $K_I = 8.5$, and $K_D = 0$ on flat sample surface. (c) is error in the amplitude estimation mode 1.

CHAPTER 4. RESULTS

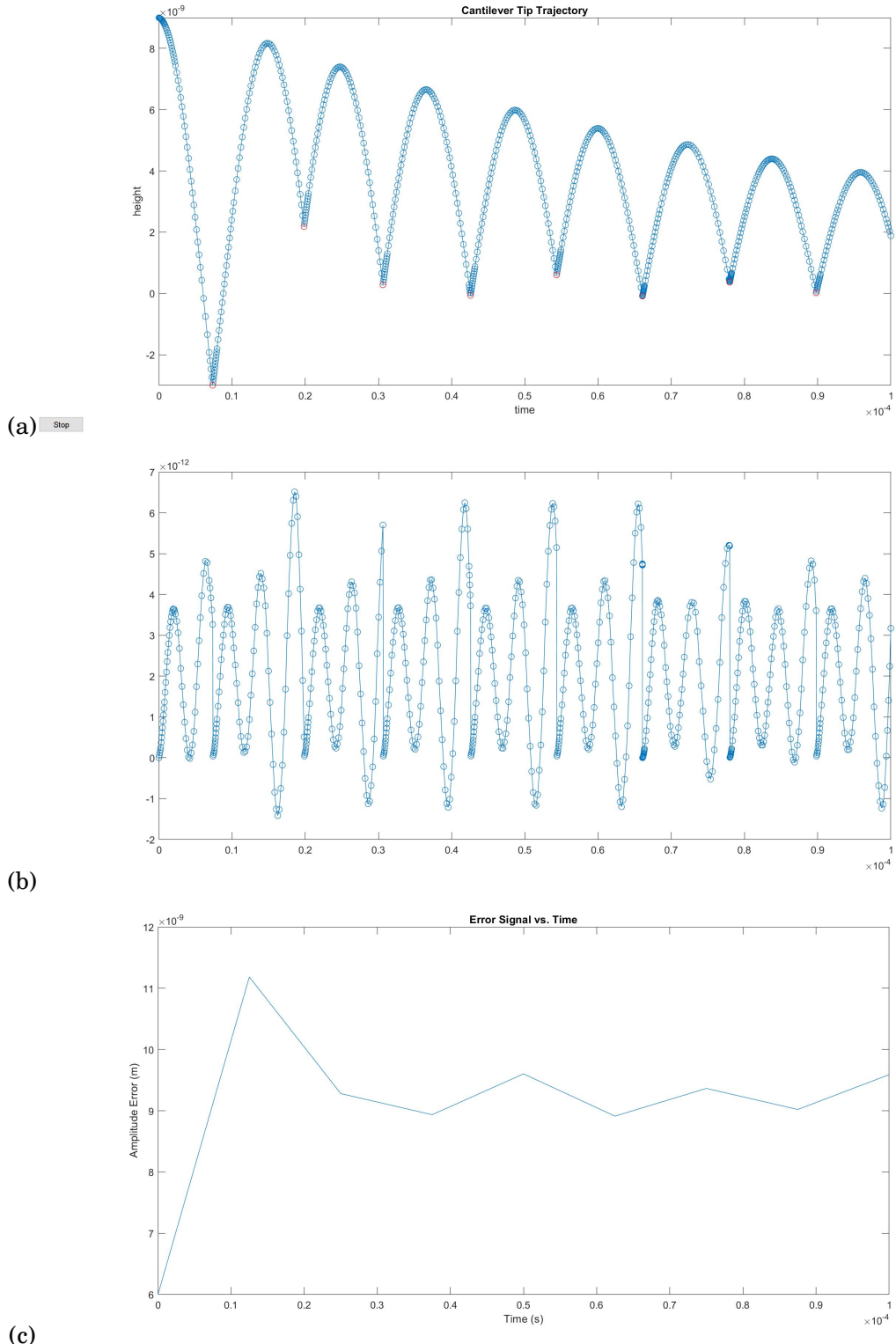


Figure 4.8: Bimodal response of (a) the first mode and (b) the second mode to PID control with gains $K_P = 0.5$, $K_I = 250$, and $K_D = 0$ on flat sample surface. (c) is error in the amplitude estimation of mode 1.

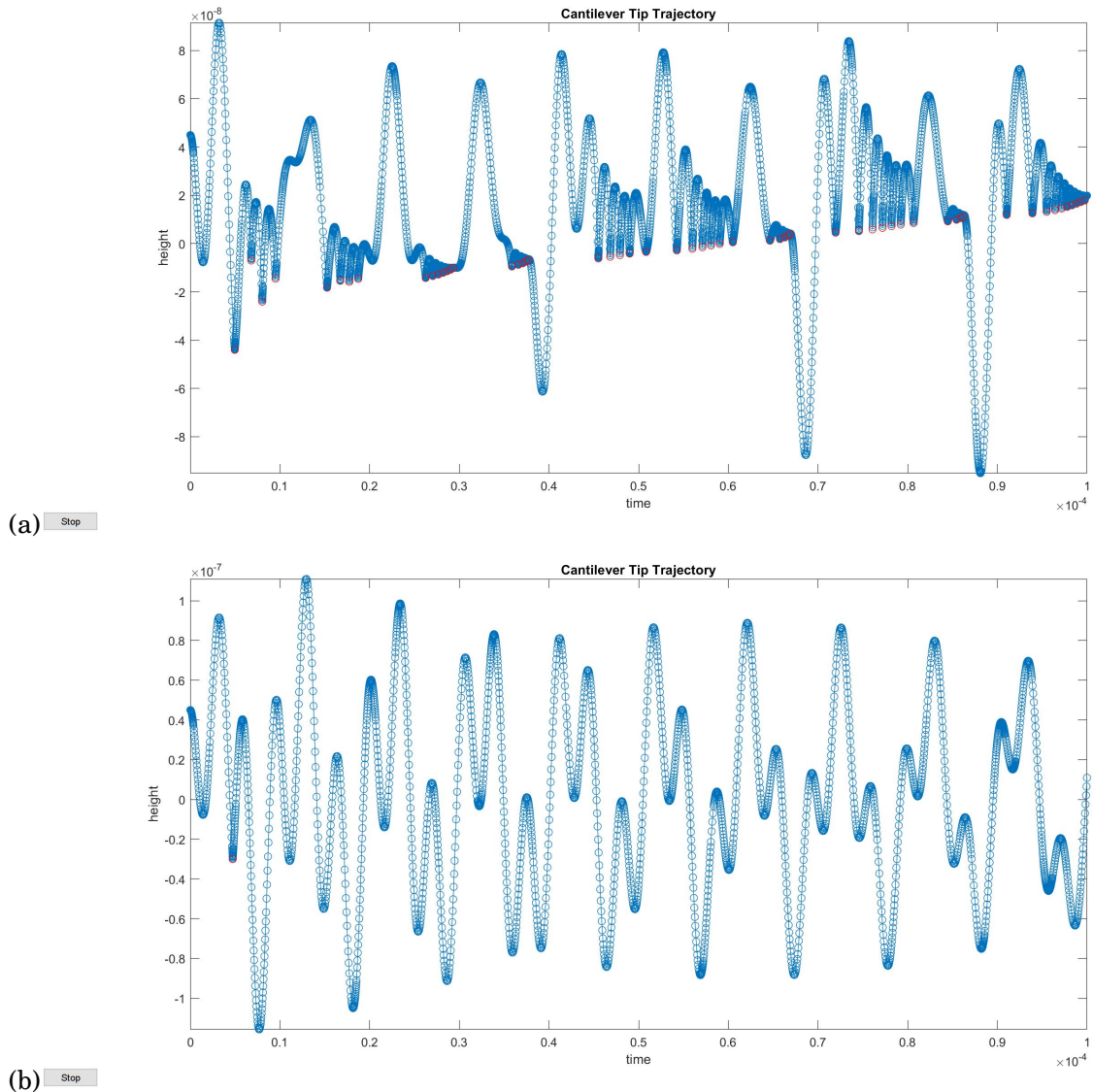


Figure 4.9: Cantilever trajectory for monomodal AFM on (a) ramp surface (4.2b), and (b) square-wave surface (4.3b) with PID gains $K_P = 0.5, K_I = 8.5, K_D = 0$.

CHAPTER 4. RESULTS

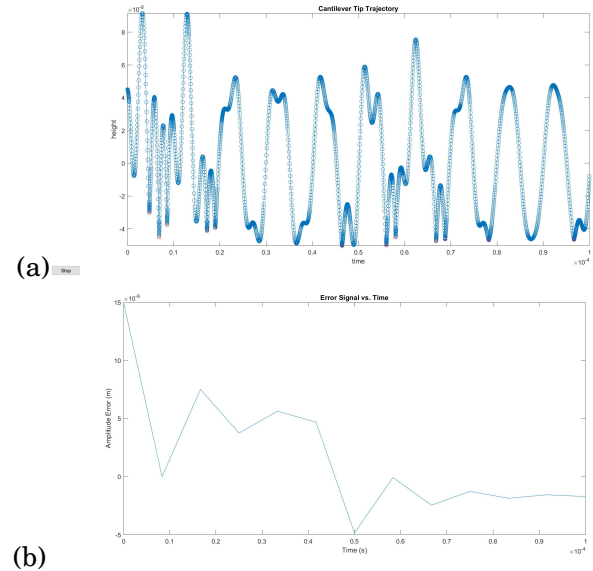


Figure 4.10: (a) Cantilever trajectory and (b) error response, respectively, for monomodal AFM on square-wave surface with $K_P = 0.5, K_I = 3.5, K_D = 0$

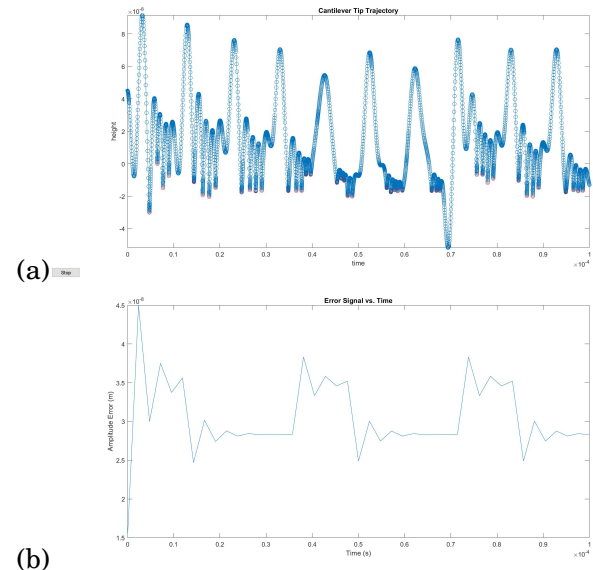


Figure 4.11: (a) Cantilever trajectory and (b) error response, respectively, for monomodal AFM on square-wave surface with $K_P = 0.5, K_I = 0.5, K_D = 0$

CHAPTER



CONCLUSION

In conclusion, this project was an exercise in numerical modelling of the recent theory of multifrequency AFM. It began by introducing the necessary mathematical prerequisites for the different components of the AFM system, as well as the feedback loop used to control it. It then described the computational implementation of the models and verified their validity by subjecting single frequency AFM to simple test samples with known surfaces and established outcome expectations within. Bimodal simulations were then executed, with the systems performance measured by the response of the error output over time as well as the mapping accuracy of the system's solutions. Finally, the simulation results were presented and analyzed.

One of the main takeaways from this project was the challenge in optimizing the PID gains K_P , K_I , and K_D . It seems almost impractical to expect one set of parameters to be able to satisfactorily manage the control task for any arbitrary specimen under examination. It brings to mind the idea of adaptive controllers that can not just actuate the piezoelectric instruments, but also self-tune its own controller gains in response to new information. Corragio et. al [4] identify many advanced control techniques, such as hybrid PID, which adopts a state machine model to sense a current working condition and update its controller gains accordingly. Another popular tactic is Q control, which attempts to mitigate the effect of probe losses by temporarily increasing the speed with which the cantilever reacts [13].

Many heuristic and application-specific examples exist for various situations. However an overall, accepted general theory of PID tuning still remains to be determined. Despite this, there are still attempts to abstract the design process and identify a consistent methodology. In [26], Shamsudhin et. al. offer a systems-theoretic approach to MF-AFM. They propose a paradigm based on in-situ experimentally identifying a transfer function for the non-linear AFM system,

CHAPTER 5. CONCLUSION

from which digital techniques can then be applied.

Overall, multifrequency AFM remains a promising field to continue to propel the nanosciences forward. It has provided molecular or atomic resolution of several material systems, while simultaneously mapping other surface properties. Its versatility, combined with its capacity for parallel processing, make it a powerful tool for the future of characterization as well as fabrication.

BIBLIOGRAPHY

- [1] D. Y. ABRAMOVITCH, S. B. ANDERSSON, L. Y. PAO, AND G. SCHITTER, *A Tutorial on the Mechanisms, Dynamics, and Control of Atomic Force Microscopes*, in Proceedings of the 2007 American Control Conference, New York City, USA, July 2007.
- [2] V. BELLITTO, ed., *Atomic Force Microscopy: Imaging, Measuring and Manipulating Surfaces at the Atomic Scale*, InTechOpen, 2012, ch. 7.
- [3] H.-J. BUTT, B. CAPPELLA, AND M. KAPPL, *Force measurements with the atomic force microscope: Technique, interpretation and applications*, Surface Science Reports, 59 (2005), pp. 1 – 152.
- [4] M. CORAGGIO, M. HOMER, O. D. PAYTON, AND M. DI BERNARDO, *Improved Control Strategies for Atomic Force Microscopes in Intermittent Contact Mode*, IEEE Transactions on Control Systems Technology, 26 (2018), pp. 1673 – 1683.
- [5] D. J. DJANAL-MANN, *Modeling and Nonlinear Dynamics for Multifrequency Atomic Force Microscopy*.
University of Bristol, 05 2020.
Preliminary Report.
- [6] D. DRAKOVA, *Theoretical modelling of scanning tunnelling microscopy, scanning tunnelling spectroscopy and atomic force microscopy*, Reports on Progress in Physics, 64 (2000), pp. 1 – 86.
- [7] M. M. EGHBAL, J. JAFARI, M. ZANDBAF, AND M. MIRZAIE, *An Analysis on Nano-scale Tip-Sample Interaction Forces in Atomic Force Microscopy*, Universal Journal of Computational Analysis, 34 (2013), pp. 33 – 39.
- [8] R. GARCIA, *Atomic Force Microscopy*, Wiley-VCH, 2010, ch. 3.
- [9] R. GARCIA AND A. S. PAULO, *Attractive and repulsive tip-sample interaction regimes in tapping-mode atomic force microscopy*, Physical Review B, 60 (1999), pp. 4961 – 4967.
- [10] R. GARCÍA AND E. T. HERRUZO, *The emergence of multifrequency force microscopy*, Nature Nanotechnology, 7 (2012), pp. 217 – 226.

BIBLIOGRAPHY

- [11] R. GARCÍA AND R. PÉREZ, *Dynamic atomic force microscopy methods*, Surface Science Reports, 47 (2002), pp. 197 – 301.
- [12] F. J. GIESSIBL, *Advances in atomic force microscopy*, Reviews of Modern Physics, 75 (2003), pp. 949 – 983.
- [13] H. HÖLSCHER AND U. D. SCHWARZ, *Theory of amplitude modulation atomic force microscopy with and without Q-Control*, International Journal of Non-Linear Mechanics, 42 (2007), pp. 608 – 625.
- [14] S. I. LEE, S. W. HOWELL, A. RAMAN, AND R. REIFENBERGER, *Nonlinear dynamic perspectives on dynamic force microscopy*, tech. rep., Purdue University, 2002.
- [15] ———, *Nonlinear dynamics of microcantilevers in tapping mode atomic force microscopy: A comparison between theory and experiment*, Physical Review B, 66 (2002), pp. 115409 1 – 10.
- [16] J. R. LOZANO AND R. GARCIA, *Theory of Multifrequency Atomic Force Microscopy*, Physical Review Letters, 100 (2008), pp. 076102 1 – 4.
- [17] F. OHNESORGE AND G. BINNIG, *True Atomic Resolution by Atomic Force Microscopy Through Repulsive and Attractive Forces*, Science, 260 (1993), pp. 1451 – 1456.
- [18] A. F. PAYAM AND M. FATHIPOUR, *Modeling and Dynamic Analysis of Atomic Force Microscope based on Euler-Bernoulli Beam Theory*, Digest Journal of Nanomaterials and Biostructures, 4 (2009), pp. 565 – 578.
- [19] A. RAMAN, J. MELCHER, AND R. TUNG, *Cantilever dynamics in atomic force microscopy*, NanoToday, 3 (2008), pp. 20 – 27.
- [20] F. J. RUBIO-SIERRA, W. M. HECKL, AND R. W. STARK, *Nanomanipulation by Atomic Force Microscopy*, Advanced Engineering Materials, 7 (2005), pp. 193 – 196.
- [21] S. RÜTZEL, S. I. LEE, AND A. RAMAN, *Nonlinear dynamics of atomic-force-microscope probes driven in Lennard-Jones potentials*, Proceedings of the Royal Society, 459 (2003), pp. 1925 – 1948.
- [22] S. M. SALAPAKA AND M. V. SALAPAKA, *Scanning Probe Microscopy*, IEEE Control Systems Magazine, 28 (2008), pp. 65 – 83.
- [23] S. SANTOS, *Phase contrast and operation regimes in multifrequency atomic force microscopy*, Applied Physics Letters, 104 (2014), pp. 143109 1 – 5.
- [24] S. SANTOS, C.-Y. LAI, T. OLUKAN, AND M. CHIESA, *Multifrequency AFM: from origins to convergence*, Nanoscale, 9 (2017), p. 5038–5043.

BIBLIOGRAPHY

- [25] L. F. SHAMPINE AND M. W. REICHELT, *The MATLAB ODE suite*, SIAM Journal on Scientific Computing, 18 (1997), pp. 1 – 22.
- [26] N. SHAMSUDHIN, H. ROTHUIZEN, B. J. NELSON, AND A. SEBASTIAN, *Multi-frequency atomic force microscopy: A system-theoretic approach*, in Proceedings of the 19th World Congress The International Federation of Automatic Control, Cape Town, South Africa, August 2014.
- [27] H. T. TOIVONEN, *Simulation of dynamical systems*.
Lecture Notes - System Simulation, 02 2010.
- [28] J. A. TURNER, S. HIRSEKORN, U. RABE, AND W. ARNOLD, *High-frequency response of atomic force microscope cantilevers*, Journal of Applied Physics, 82 (1997), pp. 966 – 979.
- [29] B. VOIGTLÄNDER, *Atomic Force Microscopy*, Springer, 2019, ch. 1.
- [30] J. ZIEGLER AND N. NICHOLS, *Optimum Settings for Automatic Controllers*, Transactions of the ASME, 64 (1942), pp. 759–768.

